

Large anomalous Hall angle in a topological semimetal candidate TbPtBi

Cite as: Appl. Phys. Lett. **118**, 031901 (2021); <https://doi.org/10.1063/5.0033707>

Submitted: 18 October 2020 . Accepted: 24 December 2020 . Published Online: 19 January 2021

 Jie Chen,  Hang Li, Bei Ding, Hongwei Zhang,  Enke Liu, and  Wenhong Wang



View Online



Export Citation



CrossMark



Your Qubits. Measured.

Meet the next generation of quantum analyzers

- Readout for up to 64 qubits
- Operation at up to 8.5 GHz, mixer-calibration-free
- Signal optimization with minimal latency

Find out more



Large anomalous Hall angle in a topological semimetal candidate TbPtBi

Cite as: Appl. Phys. Lett. **118**, 031901 (2021); doi: [10.1063/5.0033707](https://doi.org/10.1063/5.0033707)

Submitted: 18 October 2020 · Accepted: 24 December 2020 ·

Published Online: 19 January 2021



View Online



Export Citation



CrossMark

Jie Chen,^{1,2}  Hang Li,²  Bei Ding,² Hongwei Zhang,² Enke Liu,²  and Wenhong Wang^{1,2,a)} 

AFFILIATIONS

¹Songshan Lake Materials Laboratory, Dongguan, Guangdong, Dongguan 100190, China

²State Key Laboratory for Magnetism, Beijing National Laboratory for Condensed Matter Physics and Institute of Physics, Chinese Academy of Sciences, Beijing 100190, China

^{a)} Author to whom correspondence should be addressed: wenhong.wang@iphy.ac.cn

ABSTRACT

In this study, the magnetotransport properties of antiferromagnetic half-Heusler single crystals of TbPtBi, a magnetic field-induced topological semimetal with a simple band structure, were investigated. We found a nonmonotonic dependence of the anomalous Hall resistivity on the magnetic field in a strong magnetic field ($B > 7$ T), which comes from the change in the band structure caused by the Zeeman-like splitting when an external magnetic field is applied. The experimental results show that credible anomalous Hall resistivity and conductivity reach up to $0.68 \text{ m}\Omega \text{ cm}$ and $125 \Omega^{-1} \text{ cm}^{-1}$, respectively. A large anomalous Hall angle up to 33% is achieved in TbPtBi, which is comparable to a typical ferromagnetic Weyl semimetal. The analysis of the results shows that this should be attributed to the topological band around E_F and low carrier density.

Published under license by AIP Publishing. <https://doi.org/10.1063/5.0033707>

Magnetotransport properties of magnetic materials receive considerable interest because they play an important role in basic science and technological applications.¹ The Anomalous Hall Effect (AHE), as an important topic in condensed matter, contains extensive physics for their many different mechanisms,² such as the intrinsic mechanism associated with the Berry curvature in entangled Bloch electronic bands³ and the extrinsic mechanism including skew scattering^{4,5} and side jump scattering.⁶ Recently, the rapid development of magnetic topological materials has made a great contribution to AHE research. Magnetic topological materials, such as $\text{Co}_3\text{Sn}_2\text{S}_2$,^{7,8} Co_2MnGa ,⁹ Co_2MnAl ,¹⁰ Fe_3GeTe_2 ,¹¹ PrAlGe ,¹² and Mn_3Sn ,¹³ exhibit a large intrinsic AHE. All of these studies identify special band structures such as Weyl node, opened nodal line in a Weyl semimetal, or nodal line semimetal host large Berry curvature. Due to their close relationship between the topological band structure and the Berry curvature, the AHE is sensitive to the position of the topological band relative to Fermi level E_F . However, it is not easy to realize such a tunability of the band structure by direct Zeeman splitting of an external magnetic field since the change in energy is too small, on an order of several meV.¹⁴ For rare-earth element R, the interaction between localized R spins through the RKKY (Ruderman–Kittel–Kasuya–Yosida) mechanism can produce an exchange field in the 5d orbital, which causes the band to exhibit Zeeman-like splitting reaching the order of 0.1 eV.¹⁴ When

the topological band is close to E_F , the splitting will tune the band. Therefore, the dependence of the tunable AHE on magnetic field B is usually observed in rare-earth-based compounds, such as EuTiO_3 ¹ and half-Heusler compounds GdPtBi .^{15,16} As a magnetic field-induced Weyl semimetal,^{17,18} GdPtBi shows unconventional anomalous Hall effects.^{15,16}

On the other hand, as the sister compound of GdPtBi , antiferromagnetic (AFM) half-Heusler TbPtBi exhibits a large chiral anomaly induced negative magnetoresistance, the typical feature of Weyl semimetal.¹⁹ Similar to GdPtBi , TbPtBi is magnetic-field-induced Weyl semimetal that should show a large AHE. Here, in this Letter, we show the obvious abnormal behavior of the Hall resistivity under a high magnetic field ($B > 7$ T), which allows us to extract the AHE. As a result, we obtained an anomalous Hall angle (AHA) of up to 33%, which is comparable to the typical magnetic Weyl semimetal $\text{Co}_3\text{Sn}_2\text{S}_2$ ^{7,20} and full Heusler compounds $\text{Co}_2\text{MnGa/Al}$.^{9,21}

We crystallized TbPtBi single crystals by the Bi flux method^{22,23} with a molar ratio of Tb:Pt:Bi = 1:1:20. Magnetotransport and magnetic properties were measured on the Steady High-Magnetic Field Facilities in High-Magnetic Field Laboratory and Quantum Design Physical Property Measurement System (PPMS). The chemical composition was investigated by scanning electron microscopy using energy-dispersive x-ray spectrometry (EDS). We determined the

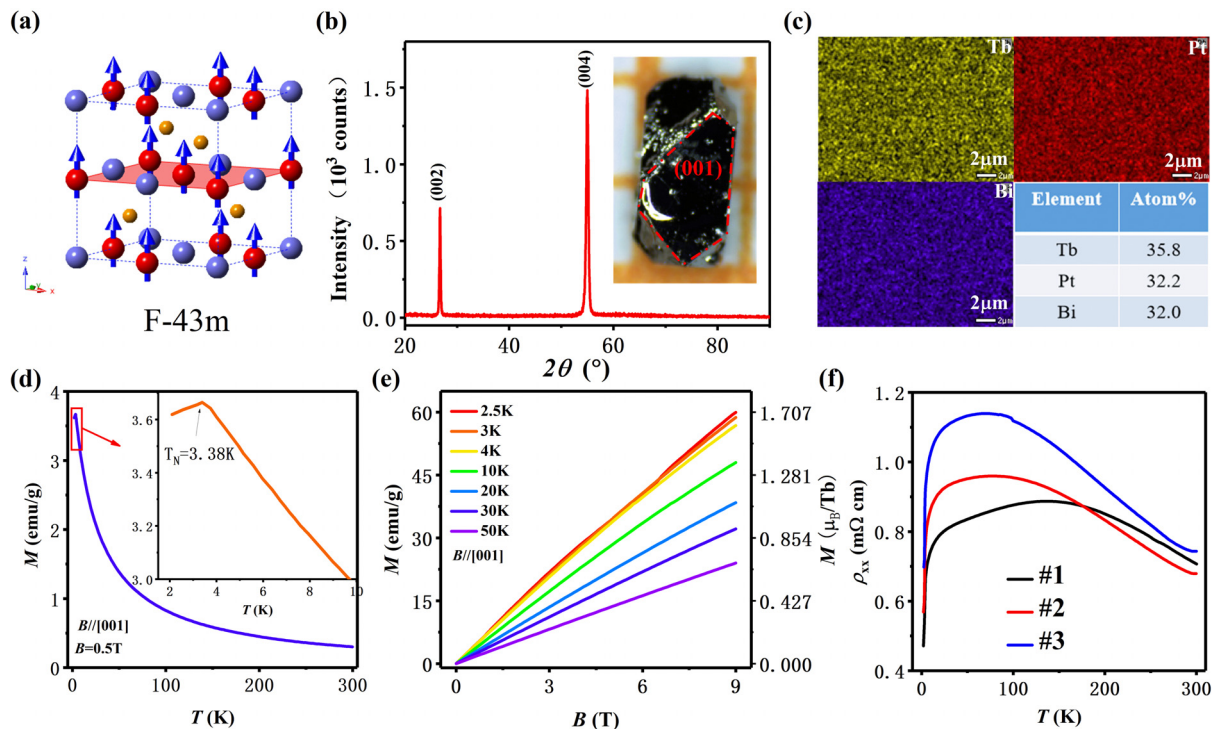


FIG. 1. Crystal structure, magnetism, and electricity characteristics of TbPtBi. (a) TbPtBi crystallized in the typical half-Heusler structure, which belongs to the F-43m (216) space group. The red ball is rare-earth atom Tb sited at (0.5, 0.5, and 0.5), which shows a ferromagnetic order in a high magnetic field. Pt (orange) and Bi (blue) site at (0.25, 0.25, and 0.25) and (0, 0, and 0), respectively. (b) X-ray diffraction pattern of TbPtBi single crystals. The inset shows an optical image of a typical sample with a (001) plane on a millimeter scale. (c) Element maps show the molar ratio of Tb:Pt:Bi = 1.11:1:1. (d) The thermal magnetization of TbPtBi at $B = 0.5T$. The inset shows the magnetization curve at $T < 10K$. (e) The isothermal magnetization data at low temperatures, measured with an external magnetic field along the [001] axis. (f) Temperature dependence of resistivity curves for three samples #1, #2, and #3 at a current $I \parallel [100]$. These three samples have the same composition and crystal orientation.

orientation of single crystals by x-ray diffraction. DFT calculations were performed using WIEN2k code.²⁴ Perdew–Burke–Ernzerhof Generalized Gradient Approximation (PBE-GGA) is used for the calculation of the exchange correlation potentials.²⁵ The large exchange

parameter $U_{\text{eff}} = 0.6 \text{ Ry}$ was applied to rare-earth elements Tb, which would shift the 4f electrons far away from the Fermi level E_F .

As shown in Fig. 1(a), TbPtBi crystallizes in an MgAgAs-type structure with a space group of F-43m and a lattice parameter of

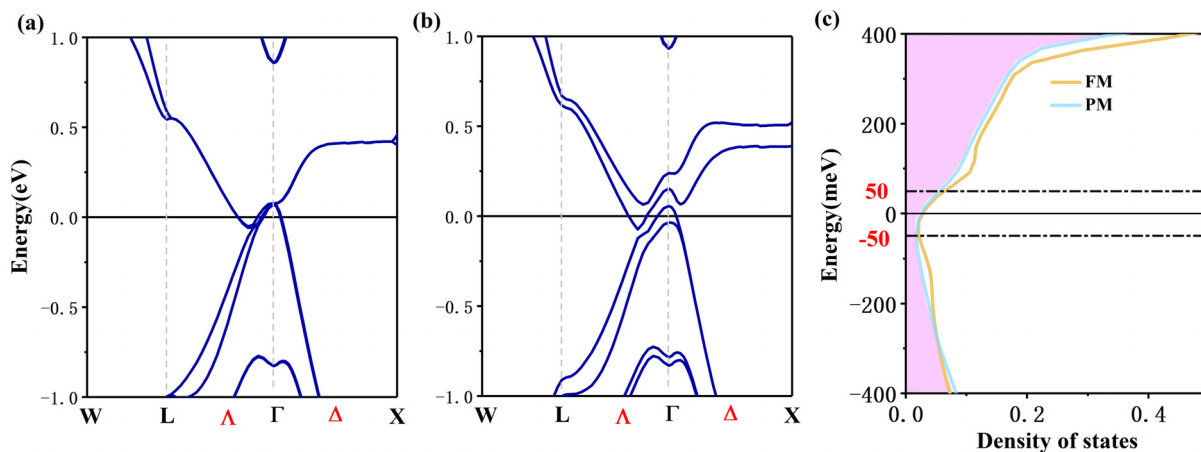


FIG. 2. Band structure and density of states of TbPtBi. The band structure for paramagnetic states (a) and ferromagnetic states (b) reproduced with permission from Chen *et al.*, Appl. Phys. Lett. 116 (22) (2020). Copyright 2020 AIP Publishing. (c) Density of states for paramagnetic states and ferromagnetic states.

$a = 6.702 \text{ \AA}$. The x-ray pattern in Fig. 1(b) identified the [001] orientation of the single crystal. The component of single crystals obtained by the Bi-flux method was detected by EDS. Figure 1(c) shows color maps of Tb, Pt, and Bi. The elements are uniformly distributed over the surface. Nonstoichiometric TbPtBi single crystals with a mole ratio of Tb:Pt:Bi = 1.11:1:1 were obtained. Figure 1(d) presents the dependence of magnetization (M) on temperature (T) at $B = 0.5 \text{ T}$ along the [001] axis, where B is the magnetic flux density. The MT curve shows an antiferromagnetic transition at 3.38 K. The enlarged magnetic transition at low T is shown in the inset. Fitting of the paramagnetic curve according to the Curie–Weiss law indicated a large effective magnetic moment of $\mu_{\text{eff}} = 9.57\mu_B$, which is close to the theoretical value of $\mu(\text{Tb}^{3+}) = 9.72\mu_B$. The isothermal magnetization curves show a linear behavior in both antiferromagnetic ($T < 3.38 \text{ K}$) and paramagnetic states. There is no metamagnetic transition in the whole magnetic field range ($B < 9 \text{ T}$). Therefore, the magnetic structure as the origin of the AHE can be excluded. Figure 1(f) shows zero-field resistivity with current $I // [100]$ for samples #1, #2, and #3. These three samples have the same composition and crystal orientation. Similar zero-field resistivity curves indicated a stable quality of single

crystals. The semiconductor-to-metallic behavior indicated a gapless semiconductor or semimetal, which coincided with the semimetallic band structure in Fig. 2.

Indeed, a detailed calculation on the band structure and topological properties of TbPtBi in various magnetic states was performed by Zhu *et al.*²⁶ The results show that TbPtBi is an AFM topological insulator, but the Weyl semimetal state will emerge when the magnetic moments of Tb are aligned along [001], because the T -range of the AHE mainly distributes in the paramagnetic state. Here, we illustrated its band structures and density of states (DOS) for paramagnetic (PM) and ferromagnetic (FM) states in Fig. 2 to show the change in the band structure and DOS under the influence of a magnetic field. In the PM state, since spin polarization is absent, the total magnetic moment is fixed to zero. As shown in Fig. 2(a), the band structure in the PM state is similar to that of no magnetic half-Heusler LuPtBi;²⁷ it shows an electron pocket and a hole pocket around the Γ point. When magnetic moment Tb is ferromagnetically aligned, the bands around the Γ point split into four bands, and the energy shift is about 0.09 eV, the electron pocket and hole pocket are still conserved. For the nonstoichiometric component of our sample, the Fermi level E_F can be

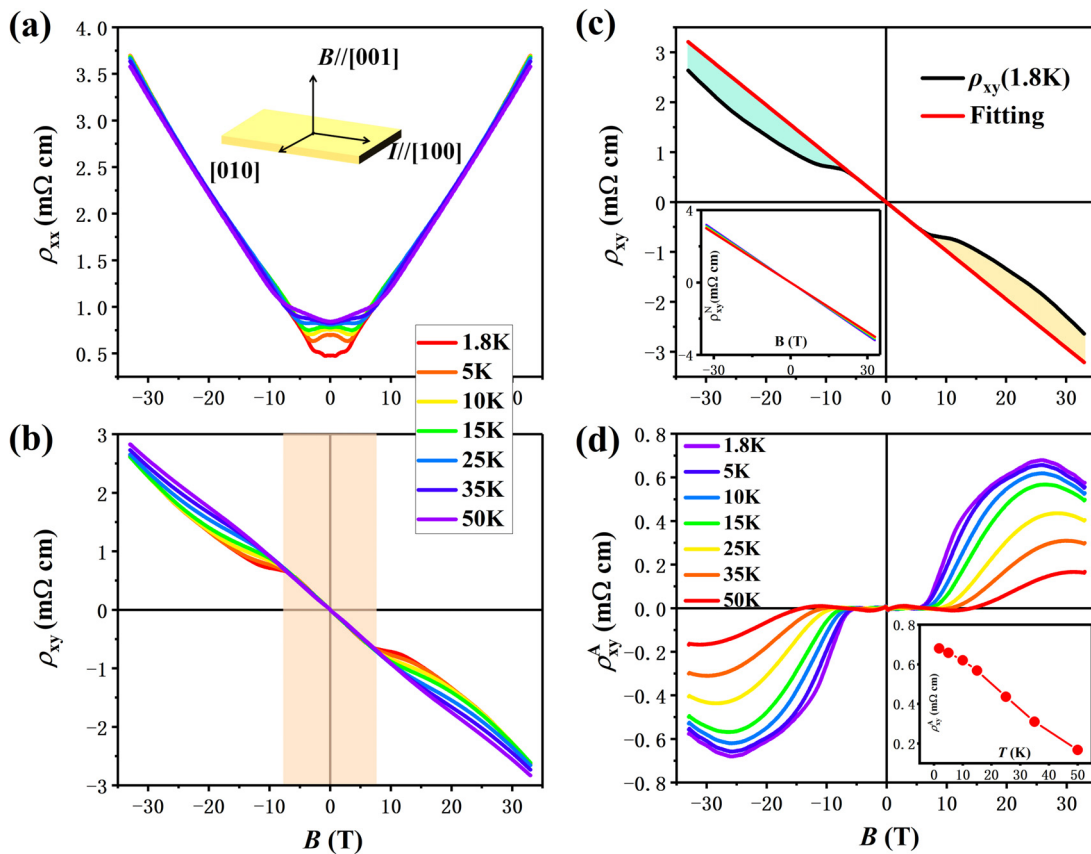


FIG. 3. Anomalous Hall effect for TbPtBi sample #1. Dependence of the longitudinal resistivity ρ_{xx} (a) and Hall resistivity ρ_{xy} (b) on magnetic field B at temperatures from 1.8 K to 50 K. The maximum magnetic field B reaches 32 T. The inset of (a) shows the geometric configuration of the external magnetic field, $B // [001]$ and the current, $I // [100]$. (c) Separation progress of normal Hall resistivity ρ_{xy}^N and anomalous Hall resistivity ρ_{xy}^A at 1.8 K. The inset shows the normal Hall resistivity obtained by linear fitting for low magnetic field curves at corresponding T . (d) The anomalous Hall resistivity ρ_{xy}^A after subtracting the fitting normal Hall resistivity ρ_{xy}^N . The inset shows the maximum value of ρ_{xy}^A at different temperatures.

shift. According to experimental results of transport, electrons dominate the electrical transport. Obviously, one carrier model indicates that E_F shifts to a high energy level. As shown in Fig. 2(c), the DOS values are almost unchanged in the range from -50 meV to 50 meV. This means that the carrier density may hold a constant value in this energy window. This conclusion makes it possible to exclude the influence of a change in carrier density in an external magnetic field.

Then, the Hall resistivity ρ_{xy} and magnetoresistance ρ_{xx} were measured on three TbPtBi samples with $B//[001]$ and $I//[100]$. Figure 3 shows the AHE and the progress of extracting ρ_{xy}^A for sample #1. Similar to other half-Heusler compounds, sample #1 [see Fig. 3(a)] shows abnormal magnetoresistance curves in a low magnetic field, which can be attributed to the quantum coherence effect.²² With the increase in the external magnetic field, electrons will decohere and return to the classical Drude model. For $\rho_{xx}(T=1.8$ K), the abnormal behavior disappears at 3 T and shows linear behavior in the higher field. Interestingly, the linear curves $\rho_{xx}(B)$ in the high field overlap for different T values. Figure 3(b) presents the Hall resistivity ρ_{xy} at B up to 32 T. In general, Hall resistivity ρ_{xy} of a magnetic material can be expressed as $\rho_{xy} = R_H B + \rho_{xy}^A$, where $R_H B$ is the normal Hall resistivity ρ_{xy}^N due to the Lorentz effect. In the light orange range ($B < 7$ T), ρ_{xy} shows a linear dependence on B , which means the normal Hall effect. With the B increase, an additional Hall signal appears, which is assumed to be anomalous Hall resistivity ρ_{xy}^A . Obviously, there is a critical field B_c for observing the AHE, and the value of B_c increases with the increase in T . For Hall resistivity at 50 K, the linear part persists up to about 15 T. This indicates that a higher B is needed to trigger an additional Hall signal for a high T . The origin of this phenomenon of the critical field can be associated with a change in the band structure.

To scale the contribution of ρ_{xy}^A , we fitted a linear curve in the light orange area for the normal Hall signal ρ_{xy}^N and extracted ρ_{xy}^A by subtracting the fit line. Figure 3(c) shows a Hall resistivity of 1.8 K as an example. Separating ρ_{xy}^A and ρ_{xy}^N is clean and reliable. The peak of $\rho_{xy}^A(1.8$ K) is 0.68 m Ω cm, which is about 3.7 times of $\rho_{xy}^A(2$ K) = 0.18 m Ω cm of GdPtBi.¹⁶ The inset shows the fitting line for normal Hall resistivities at different T values. The overlapped lines indicate that the carrier concentration n_e remained almost unchanged around $T < 50$ K. Negative Hall factors R_H imply that the carrier of electrons dominates the transport that is opposite to the hole in previous data.^{26,28} This difference can be explained by the influence of the nonstoichiometric component on the Fermi level E_F . The nonstoichiometric component may push the Fermi level slightly above the stoichiometric one. In this case, electrons dominate the transport and only the conduction bands cross the Fermi level. The obtained carrier concentration n_e and mobility μ_e are shown in Table S1. The carrier concentration and mobility can reach $n_e = 6.41 \times 10^{18}$ cm $^{-3}$ and $\mu_e = 2037$ cm $^{-2}$ V $^{-1}$ s $^{-1}$ at 1.8 K. n_e is of the same order as the other half-Heusler RPtBi, but about half of the previous result is $n_h = 1.2 \times 10^{19}$ cm $^{-3}$ in TbPtBi.²⁸ Figure 3(d) shows the extracted ρ_{xy}^A for different T and B values. In the range of $B > 7$ T, strong swells were observed, which persisted to 32 T. The inset shows the maximum values of ρ_{xy}^A for corresponding T , and ρ_{xy}^A decreases rapidly with increasing T .

To further characterize the AHE in TbPtBi, we used two characteristic parameters: anomalous Hall conductivity σ_{xy}^A (AHC) and AHA. The AHC is given as $\sigma_{xy}^A = -\rho_{xy}^A/(\rho_{xy}^2 + \rho_{xx}^2)$, which is the absolute scale of the AHE. Figure 4(a) shows the dependence of σ_{xy}^A on

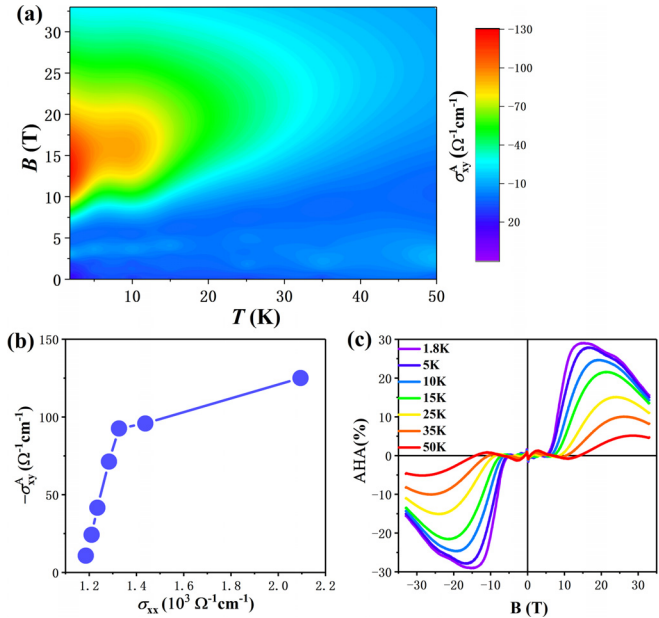


FIG. 4. Anomalous Hall conductivity σ_{xy}^A and AHA for sample #1. (a) Color plot of anomalous Hall conductivity σ_{xy}^A for 1.8 K $< T < 50$ K and 0 T $< B < 32$ T. (b) Scaling of the anomalous Hall conductivity σ_{xy}^A as a function of σ_{xx} for various temperatures. (c) Anomalous Hall angle (AHA).

T and B . The orange area represents the large anomalous Hall conductivity σ_{xy}^A . Compared to GdPtBi's result,¹⁶ σ_{xy}^A mainly distributes in a higher field range, 10 T $< B < 22$ T and the maximum of σ_{xy}^A reaches -125 Ω^{-1} cm $^{-1}$. Figure 4(b) shows the σ_{xy}^A vs σ_{xx} curve for the T -range of 1.8–50 K. We find that the relationship between σ_{xy}^A and σ_{xx} can be divided into two parts. In the range of $T > 10$ K, σ_{xy}^A shows a strong dependence on σ_{xx} . However, σ_{xy}^A is almost independent of σ_{xx} below $T = 10$ K. This feature is consistent with the intrinsic AHE mechanism. The AHA is another parameter for scaling the AHE, defined by the ratio of $\sigma_{xy}^A/\sigma_{xx}$, which measures the relative contribution of the anomalous Hall current in relation to the longitudinal current.² TbPtBi, as a magnetic topological semimetal candidate, may feature a giant anomalous Hall angle due to its special band structure. Figure 4(c) shows AHA vs T and B . Similar to anomalous Hall resistivity, the AHA in the low field is close to zero. The AHA shows a swell when $B > 7$ T. With decreasing T , the AHA increases sharply from 5.1% at 50 K to a maximum of 29% at 1.8 K and 15 T for sample #1.

In Fig. 5, we list the AHAs in these famous compounds with a large AHE. By comparison, we know that most of the systems have a tiny AHA. Only a few of the materials are of great value, for example, magnetic Weyl semimetal $\text{Co}_3\text{Sn}_2\text{S}_2$ ^{7,20} and full-Heusler compounds $\text{Co}_2\text{MnGa/Al}$.^{9,21} Magnetic half-Heusler compounds RPtBi (such as GdPtBi and TbPtBi) are another system with a giant AHA. The common features of these systems are the topological band structure near the Fermi level and semimetallic band. As we all know, the topological band structure contributes greatly to the intrinsic AHC for their strong Berry curvature. The semimetallic band guarantees the low carrier density and low longitudinal conductivity. Both features are required

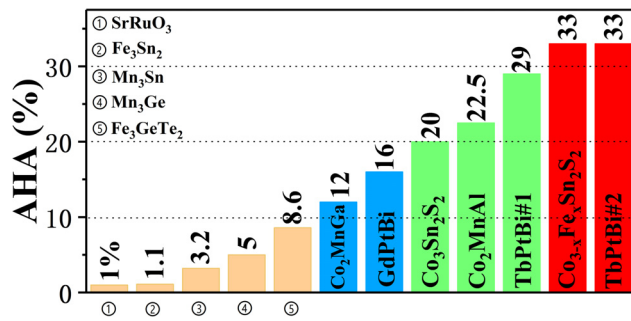


FIG. 5. Comparison of our anomalous Hall angle with the one for other AHE materials. Dashed lines represent AHA = 10%, 20%, and 30%. The data shown are taken from Refs. 7, 9–11, 13, 16, 20, and 29–31.

to produce a giant AHA. For observation of chiral anomaly negative magnetoresistance, TbPtBi is regarded as a magnetic field-induced Weyl semimetal. However, we need to point out that TbPtBi is not an intrinsic ferromagnetic compound, instead of a magnetic field-induced ferromagnetic order. This feature makes the AHE exist in a high magnetic field, which is a disadvantage for applications. Therefore, reducing the critical field B_c for the AHE is the next key challenge for implementation of applications. Reducing the lattice parameter or replacing Tb with Ho may effectively reduce the critical field.

See the [supplementary material](#) for list of carrier density n_c , mobility μ_c , the maximum value of anomalous Hall resistivity, anomalous Hall conductivity, and anomalous Hall angle for sample #1 at different T in Table S1 and Hall resistivity, magnetoresistance, anomalous Hall resistivity, and AHA for sample #2 in Fig. S1.

This work was supported by the National Science Foundation of China (Nos. 11974406 and 12074415) and the China Postdoctoral Science Foundation (No. 2020M680734). A portion of this work was performed on the Steady High Magnetic Field Facilities, High Magnetic Field Laboratory, Chinese Academy of Science.

DATA AVAILABILITY

The data that support the finding of this study are available within this article.

REFERENCES

- K. S. Takahashi, H. Ishizuka, T. Murata, Q. Y. Wang, Y. Tokura, N. Nagaosa, and M. Kawasaki, *Sci. Adv.* **4**, eaar7880 (2018).
- N. Nagaosa, J. Sinova, S. Onoda, A. H. MacDonald, and N. P. Ong, *Rev. Mod. Phys.* **82**(2), 1539 (2010).
- R. Karplus and J. M. Luttinger, *Phys. Rev.* **95**(5), 1154 (1954).
- J. Smit, *Physica* **24**, 39 (1958).
- J. Smit, *Physica* **21**, 877 (1955).
- L. Berger, *Phys. Rev. B* **2**(11), 4559 (1970).

- E. Liu, Y. Sun, N. Kumar, L. Muechler, A. Sun, L. Jiao, S.-Y. Yang, D. Liu, A. Liang, Q. Xu, J. Kroder, V. Süß, H. Borrmann, C. Shekhar, Z. Wang, C. Xi, W. Wang, W. Schnelle, S. Wirth, Y. Chen, S. T. B. Goennenwein, and C. Felser, *Nat. Phys.* **14**, 1125 (2018).
- Q. Wang, Y. Xu, R. Lou, Z. Liu, M. Li, Y. Huang, D. Shen, H. Weng, S. Wang, and H. Lei, *Nat. Commun.* **9**(1), 3681 (2018).
- A. Sakai, Y. P. Mizuta, A. A. Nugroho, R. Sihombing, T. Koretsune, M.-T. Suzuki, N. Takemori, R. Ishii, D. Nishio-Hamane, R. Arita, P. Goswami, and S. Nakatsuji, *Nat. Phys.* **14**(11), 1119 (2018).
- P. Li, J. Koo, W. Ning, J. Li, L. Miao, L. Min, Y. Zhu, Y. Wang, N. Alem, C. X. Liu, Z. Mao, and B. Yan, *Nat. Commun.* **11**(1), 3476 (2020).
- K. Kim, J. Seo, E. Lee, K. T. Ko, B. S. Kim, B. G. Jang, J. M. Ok, J. Lee, Y. J. Jo, W. Kang, J. H. Shim, C. Kim, H. W. Yeom, B. I. Min, B. J. Yang, and J. S. Kim, *Nat. Mater.* **17**(9), 794 (2018).
- B. Meng, H. Wu, Y. Qiu, C. Wang, Y. Liu, Z. Xia, S. Yuan, H. Chang, and Z. Tian, *APL Mater.* **7**(5), 051110 (2019).
- S. Nakatsuji, N. Kiyohara, and T. Higo, *Nature* **527**(7577), 212 (2015).
- N. Kozlova, J. Hagel, M. Doerr, J. Wosnitza, D. Eckert, K. H. Müller, L. Schultz, I. Opahle, S. Elgazzar, M. Richter, G. Goll, H. von Lohneysen, G. Zwicky, T. Yoshino, and T. Takabatake, *Phys. Rev. Lett.* **95**(8), 086403 (2005).
- C. Shekhar, N. Kumar, V. Grinenko, S. Singh, R. Sarkar, H. Luetkens, S.-C. Wu, Y. Zhang, A. C. Komarek, E. Kampert, Y. Skourski, J. Wosnitza, W. Schnelle, A. McCollam, U. Zeitler, J. Kübler, B. Yan, H.-H. Klaus, S. S. P. Parkin, and C. Felser, *Proc. Natl. Acad. Sci. U. S. A.* **115**(37), 9140 (2018).
- T. Suzuki, R. Chisnell, A. Devarakonda, Y. T. Liu, W. Feng, D. Xiao, J. W. Lynn, and J. G. Checkelsky, *Nat. Phys.* **12**(12), 1119 (2016).
- C. Felser and B. Yan, *Nat. Mater.* **15**(11), 1149 (2016).
- J. Cano, B. Bradlyn, Z. Wang, M. Hirschberger, N. P. Ong, and B. A. Bernevig, *Phys. Rev. B* **95**(16), 161306(R) (2017).
- J. Chen, H. Li, B. Ding, E. Liu, Y. Yao, G. Wu, and W. Wang, *Appl. Phys. Lett.* **116**(22), 222403 (2020).
- J. Shen, Q. Zeng, S. Zhang, H. Sun, Q. Yao, X. Xi, W. Wang, G. Wu, B. Shen, Q. Liu, and E. Liu, *Adv. Funct. Mater.* **30**, 2000830 (2020).
- P. Li, J. Koo, W. Ning, J. Li, L. Miao, L. Min, Y. Zhu, Y. Wang, N. Alem, C.-X. Liu, Z. Mao, and B. Yan, [arXiv:1910.10378v1](#) (2019).
- J. Chen, H. Li, B. Ding, Z. Hou, E. Liu, X. Xi, G. Wu, and W. Wang, *Appl. Phys. Lett.* **116**(10), 101902 (2020).
- J. Chen, H. Li, B. Ding, Z. Hou, E. Liu, X. Xi, H. Zhang, G. Wu, and W. Wang, *J. Alloys Compd.* **784**, 822 (2019).
- P. Blaha, K. Schwarz, G. Madsen, D. Kvasnicka, and J. Luitz, “WIEN2K, an augmented plane wave \hat{o} \hat{u} \hat{o} flocal orbitals program for calculating crystal properties” (Karlheinz Schwarz Technische Universitaet Wien, Wien, Austria, 2001).
- P. Perdew, K. Burke, and M. Ernzerhof, *Phys. Rev. Lett.* **77**(18), 3865 (1996).
- Y. Zhu, B. Singh, Y. Wang, C.-Y. Huang, W.-C. Chiu, B. Wang, D. Graf, Y. Zhang, H. Lin, J. Sun, A. Bansil, and Z. Mao, *Phys. Rev. B* **101**(16), 161105(R) (2020).
- Z. Hou, W. Wang, G. Xu, X. Zhang, Z. Wei, S. Shen, E. Liu, Y. Yao, Y. Chai, Y. Sun, X. Xi, W. Wang, Z. Liu, G. Wu, and X.-X. Zhang, *Phys. Rev. B* **92**(23), 235134 (2015).
- R. Singha, S. Roy, A. Pariari, B. Satpati, and P. Mandal, *Phys. Rev. B* **99**(3), 035110 (2019).
- Z. Fang, N. Nagaosa, K. S. Takahashi, A. Asamitsu, R. Mathieu, T. Ogasawara, H. Yamada, M. Kawasaki, Y. Tokura, and K. Terakura, *Science* **302**(5642), 92 (2003).
- L. Ye, M. Kang, J. Liu, F. von Cube, C. R. Wicker, T. Suzuki, C. Jozwiak, A. Bostwick, E. Rotenberg, D. C. Bell, L. Fu, R. Comin, and J. G. Checkelsky, *Nature* **555**(7698), 638 (2018).
- A. K. Nayak, J. E. Fischer, Y. Sun, B. Yan, J. Karel, A. C. Komarek, C. Shekhar, N. Kumar, W. Schnelle, J. Kübler, C. Felser, and S. S. P. Parkin, *Sci. Adv.* **2**, e1501870 (2016).